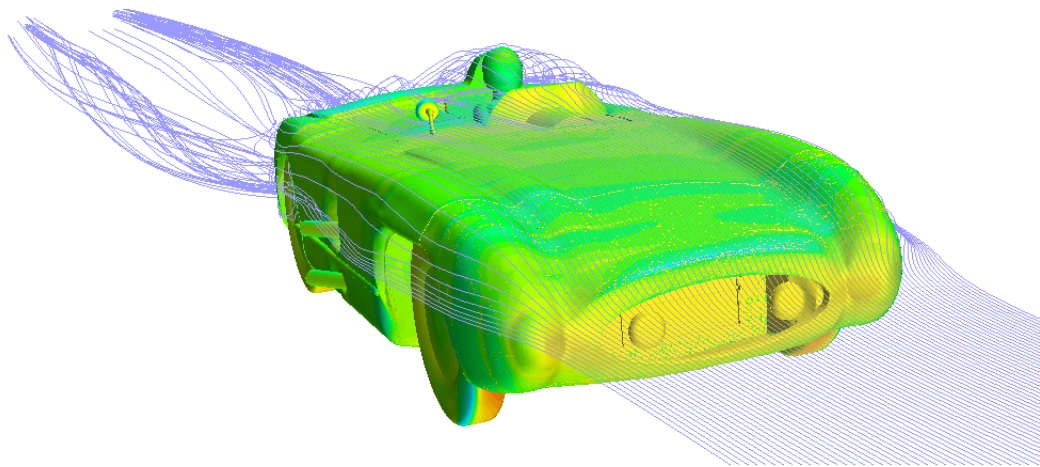


# CHALMERS



## **CFD-analysis of the aerodynamic properties of a Mercedes-Benz 300SLR**

Bachelor's thesis in Applied Mechanics

ANDREAS FALKOVÉN  
JOHAN NORDIN  
KRESHNIK RAMA  
ANDREAS RASK  
PHILIP SJÖSTRAND  
MICHAEL STADLER

Department of Applied Mechanics  
Division of Vehicle Engineering and Autonomous Systems  
CHALMERS UNIVERSITY OF TECHNOLOGY  
Gothenburg, Sweden 2015  
Bachelor thesis nr 2015:07



BACHELOR'S PROJECT TMEX02-15-15

# CFD-analysis of the aerodynamic properties of a Mercedes-Benz 300SLR

Comparison of drag- and lift forces generated when the Mercedes' air  
brake is deployed

ANDREAS FALKOVÉN  
JOHAN NORDIN  
KRESHNIK RAMA  
ANDREAS RASK  
PHILIP SJÖSTRAND  
MICHAEL STADLER



**CHALMERS**  
UNIVERSITY OF TECHNOLOGY

Department of Applied Mechanics  
*Division of Vehicle Engineering and Autonomous Systems*  
CHALMERS UNIVERSITY OF TECHNOLOGY  
Gothenburg, Sweden 2015

CFD-analysis of the aerodynamic properties of a Mercedes-Benz 300SLR.  
Comparison of drag- and lift forces generated when the Mercedes' air brake is de-  
ployed.

ANDREAS FALKOVÉN  
JOHAN NORDIN  
KRESHNIK RAMA  
ANDREAS RASK  
PHILIP SJÖSTRAND  
MICHAEL STADLER

© ANDREAS FALKOVÉN JOHAN NORDIN KRESHNIK RAMA ANDREAS  
RASK PHILIP SJÖSTRAND MICHAEL STADLER, 2015.

Supervisor: Emil Ljungskog  
Examiner: Professor Lennart Löfdahl

Bachelor's project TMEX02-15-15  
Department of Applied Mechanics  
Division of Vehicle Engineering and Autonomous Systems  
Chalmers University of Technology  
SE-412 96 Gothenburg  
Telephone +46 31 772 1000

Cover: Streamlines around the Mercedes-Benz 300SLR travelling at 120 kph.

Gothenburg, Sweden 2015

## Abstract

Mercedes-Benz was one of the most prominent car manufacturers in motorsport in the 50's. In 1955 they participated with the model 300 SLR in the Le Mans 24-hour race. What made this model standing out was the mounted air brake, which would compensate for the weaker drum brakes compared with competing models' disc brakes. During the ongoing race the world became witness to one of the most fatal accident in motorsport history, where the Mercedes in a collision flew up and crashed into the grandstand.

The aim of this work was to investigate the air brake's effect on the car's characteristics at the crash moment. This is done by monitoring the work of Peter Gullberg and Lennart Löfdahl performed in 2008, but with a more accurate basis.

A laser scanned model of the car that was obtained from Gullbergs and Löfdahl's work in 2008 was improved to match more with the real car and to obtain accurate results in the flow simulations performed in STAR CCM+.

The results obtained confirmed the earlier work in the field which indicated that the car gets an overall higher downforce with the air brake engaged compared to the down position. Additionally, a major downforce was noted on the rear axle compared to the front when the air brake was engaged.

## Sammanfattning

Mercedes-Benz var en av de absolut främsta biltillverkarna inom motorsporten på 50-talet. År 1955 deltog de med modellen 300 SLR i Le Mans 24-timmarslopp. Vad som stack ut med denna modell var att det monterats en luftbroms för att kompensera för de svagare trumbromsarna jämfört med konkurrerande modellers skivbromsar. Under loppet skedde den mest fatala olyckan i motorsportens historia, där Mercedesen vid en kollision flög upp och kraschade in i åskådarläktaren.

Syftet med arbetet var att utreda luftbromsens inverkan på bilens egenskaper vid kraschtillfället. Detta görs genom uppföljning av det arbete Peter Gullberg och Lennart Löfdahl utfört 2008, men med noggrannare underlag.

En laserskannad modell av bilen som erhöles från Gullbergs och Löfdahls arbete 2008 importerades och gjordes mer noggran som den riktiga bilen för att sedan erhålla noggrannare resultat vid de strömningssimuleringar som utförts i STAR CCM+.

De resultat som erhöles bekräftar det tidigare arbetets indikationer att bilen får en ökad total downforce vid uppfälld luftbroms jämfört med nedfälld. Dessutom noteras en större downforce på bakaxeln jämfört med framaxeln då luftbromsen är uppfälld.

Keywords: CFD, mercedes, air brake, le mans, aerodynamics, drag force, lift force.



## Preface

This report represents the final results of a bachelor thesis during the period of 2015-01-27 to 2015-06-01 at the Department of Applied Mechanics at Chalmers University of Technology, Gothenburg Sweden. The objective of this project was, with the base of earlier studies made by Peter Gullberg and Lennart Löfdahl in 2008, to enhance the underlying CAD-model and analyse the aerodynamic properties of the Mercedes-Benz 300 SLR from 1955. Analysis of the aerodynamic properties of different car setups and velocities was performed using the commercial CFD-software program STAR CCM+.

It is recommended that the reader of this thesis be familiar with the basic principles of fluid dynamics to fully appreciate the contents of the report.

## Acknowledgements

First of all we would like to thank Professor Lennart Löfdahl for the opportunity to work with this project and for letting us take part of his earlier studies done in this field. His enthusiasm on the subject has been a great inspiration and motivation.

Secondly, we would like to thank our supervisor Ph.D student Emil Ljungskog for his support and excellent availability through this project. Without his aid the first simulations would probably still be running. We would also like to thank Ph.D student Teddy Hobeika for his useful opinions and tips during the simulations.

Lastly a big thank to CD-Adapco for providing us with a STAR-CCM+ license and the ability to participate in their online courses.

The authors, Gothenburg, May 2015



# Contents

<b>Nomenclature</b>	<b>xi</b>
<b>1 Introduction</b>	<b>1</b>
1.1 Historical Background . . . . .	1
1.1.1 The 1955 Le Mans tragedy . . . . .	1
1.1.2 Mercedes-Benz 300 SLR . . . . .	2
1.2 Objective . . . . .	2
1.3 Delimitations . . . . .	3
<b>2 Theory of Fluid Mechanics</b>	<b>5</b>
2.1 Reynolds transport theorem . . . . .	5
2.2 Conservation of mass and momentum in a fluid . . . . .	5
2.3 Reynolds number . . . . .	6
2.4 Compressible and incompressible flow . . . . .	6
2.5 Bernoulli's Equation . . . . .	7
2.6 Aerodynamics . . . . .	7
2.6.1 Drag and lift forces . . . . .	8
2.6.2 Laminar and turbulent flow . . . . .	8
2.7 Navier-Stokes equations . . . . .	8
2.8 Boundary layer theory . . . . .	8
2.8.1 Attached and separated flow . . . . .	9
2.9 Turbulence modelling . . . . .	9
2.9.1 Reynolds Averaged Navier-Stokes . . . . .	10
2.9.2 Realizable $k$ - $\epsilon$ model . . . . .	10
2.9.3 Modelling of porous media . . . . .	11
2.9.4 Wall treatment . . . . .	11
2.10 The Finite Volume Method . . . . .	11
<b>3 Method</b>	<b>13</b>
3.1 Pre-processing . . . . .	13
3.1.1 Preparing the laser-scan . . . . .	13
3.1.2 Modelling of the car body and air brake . . . . .	14
3.1.3 Modelling of exterior parts . . . . .	15
3.1.4 Modelling the internal parts . . . . .	16
3.1.5 Merging the model . . . . .	17
3.1.6 Surface wrapping and meshing . . . . .	18

3.2	CFD simulations . . . . .	20
3.2.1	Boundary conditions . . . . .	20
3.2.2	Physics settings . . . . .	21
3.3	Post-processing . . . . .	21
<b>4</b>	<b>Results of CFD simulations</b>	<b>23</b>
4.1	Closed cooling . . . . .	23
4.2	Open cooling . . . . .	24
<b>5</b>	<b>Discussion and Analysis</b>	<b>27</b>
5.1	Comments on methodology . . . . .	27
5.1.1	Pre processing . . . . .	27
5.1.2	Solving . . . . .	28
5.1.3	Post processing . . . . .	28
5.2	Drag forces . . . . .	28
5.3	Lift force . . . . .	29
5.4	Sources of errors . . . . .	29
5.5	Comparison with earlier works . . . . .	30
<b>6</b>	<b>Conclusions</b>	<b>33</b>
6.1	Conclusions of this project . . . . .	33
6.2	Closing remarks and future works . . . . .	33
	<b>Bibliography</b>	<b>35</b>
<b>A</b>	<b>CAD models</b>	<b>I</b>
<b>B</b>	<b>PID's</b>	<b>III</b>

## Nomenclature

<b>ANSA</b>	Pre-processing software
<b>CATIA</b>	CAD-software used to create computer models
<b>STAR CCM+</b>	CFD-software used to run simulations of fluid flow
<b>CAD</b>	Computer Aided Design
<b>CFD</b>	Computational Fluid Dynamics
<b>PID</b>	Property ID
<b>RANS</b>	Reynolds Averaged Navier Stokes
$A_p$	Characteristic area
$\alpha$	Viscous resistance in a porous medium
$a_s$	Speed of sound
$B$	An extensive property of a fluid
$\beta$	The derivative of a property $B$ with respect to its mass $m$
$\beta_I$	Inertial resistance of a porous medium
$C_D$	Coefficient of drag
$C_L$	Coefficient of lift
$C_\mu$	Dimensionless structure factor
$\frac{D}{Dt}$	Material derivative
$\delta$	Boundary layer thickness
$\delta_{ij}$	Kronecker delta
$\epsilon$	Energy dissipation factor
$F_D$	Horizontal drag force
$F_L$	Vertical lift force
$g$	Gravitational acceleration
$k$	Turbulent energy
<b>L</b>	Characteristic length
$m$	Mass
<b>Ma</b>	Mach number
$\mu$	Dynamic viscosity
$\mu_t$	Eddy viscosity
$\nu$	Kinematic viscosity

$\nabla$	Gradient operator
$p$	Pressure
$\bar{p}$	Time-averaged pressure
$p'$	Time-fluctuating pressure
<b>Re</b>	Reynolds number
$S_{ij}$	Mean flow strain rate tensor
$\tau_w$	Wall shear stress
<b>u</b>	Velocity field of a flow
$\bar{\mathbf{u}}$	Time-averaged velocity field
$U$	Free stream velocity
$u$	Flow velocity component in the $x$ -direction
$\bar{u}$	Time-averaged velocity component in the $x$ -direction
$u'$	Fluctuating velocity component in the $x$ -direction
<b>u*</b>	Friction velocity
<b>u<sup>+</sup></b>	Dimensionless velocity near a wall
$v$	Flow velocity component in the $y$ -direction
$\bar{v}$	Time-averaged velocity component in the $y$ -direction
$v'$	Fluctuating velocity component in the $y$ -direction
<b>W</b>	Parameter in the realizable $k$ - $\epsilon$ model
$w$	Flow velocity component in the $z$ -direction
$\bar{w}$	Time-averaged velocity component in the $z$ -direction
$w'$	Fluctuating velocity component in the $z$ -direction
$y^+$	Dimensionless wall distance

# 1

## Introduction

This project's focus was to run more accurate simulations of the aerodynamics of the Mercedes-Benz 300 SLR than what earlier has been done by Peter Gullberg and Lennart Löfdahl in 2008. To achieve this, a model with higher level of detail needed to be made. After successfully simulating the refined model, a comparison with Gullberg's and Löfdahl's results was done.

The Mercedes-Benz 300 SLR was run at the Le Mans race in 1955, equipped with an air brake to generate increased braking. The air brake makes the SLR an intriguing vehicle for CFD, or Computational Fluid Dynamics, analysis. This was recognised by Peter Gullberg and Lennart Löfdahl who performed preliminary CFD simulations on the SLR in 2008. Those simulations showed that “the air brake generates a significant drag increase and a downforce on the rear part of the vehicle” while engaged [1]. The increase in drag is not very surprising as this was the original purpose of the air brake. The observed downforce however is very interesting since this could explain the improved handling of the car described by the Mercedes works drivers of that time. A downforce generates extra grip which implies more efficient braking and better cornering.

### 1.1 Historical Background

*This section consists of a short summary of the history of the Mercedes-Benz 300 SLR and its role in the 1955 Le Mans disaster. For a detailed analysis on the crash, as well as the whole history of the 24-hour race of Le Mans and the aftermath of the accident, the reader is referred to the book “Le Mans '55: The crash that changed the face of motor racing” by Christopher Hilton [2].*

#### 1.1.1 The 1955 Le Mans tragedy

The Le Mans 24-hour race on June 11 1955 is barely two and a half hours old as the lead cars approach the pit straight to complete the 35th lap. Leading the race is Mike Hawthorn in a Jaguar C-type, closely followed by Juan Miguel Fangio in a Mercedes-Benz 300 SLR. Hawthorn has just passed Lance Macklin in the much slower Austin Healey when he suddenly pulls the Jaguar to the right-hand side of the track, right in front of Macklin, to enter the pits for change of drivers and refuelling.

The Jaguars brake lights turns on as Hawthorn slows down for the pit stop and Macklin, whose brakes are not nearly as effective as Hawthorns has to swerve to the left to avoid crashing into the Jaguar. From behind comes Juan Manuel Fangio and Pierre Lavegh, also in a SLR, at full speed. Lavegh cannot avoid the Austin Healey suddenly appearing in front of him and the disaster takes its cause. Lavegh hits Macklin at approximately 240 kph and the Austin Healey acts as a ramp catapulting the 300 SLR into the air. After flying about 70 meters the SLR hits a concrete tunnel where it explodes and the debris is thrown into the densely packed crowd in the grandstand. The crash was captured on camera from several angles, see for example <https://www.youtube.com/watch?v=JEk85gKJN6k>.

The 1955 Le Mans disaster remains until today the most fatal accident in motorsport history, with official reports suggesting between 80-120 dead [3]. Such a tragedy has of course had a major impact on the future development of motorsport. Even though the race actually continued after the accident, Mercedes withdrew their remaining two cars and shortly afterwards retired from Grand Prix racing altogether not to return until 1980.

### 1.1.2 Mercedes-Benz 300 SLR

Mercedes withdrawal came at a time when they were one of the dominating teams, if not *the* dominating team, in motorsport. Fangio won the Grand Prix World Championship 1955 in a Mercedes and the company had also secured first place in that year's World Sportscar Championship. Mercedes gained a reputation as a manufacture of the best and most modern race cars as a result of their recent success. The 300 SLR, for *Sport Leicht Rennen* or *Sport Light Racing* in english, was no exception. According to Stirling Moss who partnered Fangio at Le Mans 1955 the SLR was "The greatest sports racing car ever built - really an unbelievable machine."

The main features of the SLR included a fuel-injected 3 litre straight 8 engine generating 306 horsepower, ultra-light magnesium-alloy bodywork and desmodromic valves [3]. The Mercedes had a top speed of 300 kph and accelerated from 0-100 kph in 7.2 seconds [4]. However, the SLR had one major flaw: its out-of-date drum-brakes. To compensate for the cars lack of braking power, prior to the Le Mans '55, the SLR was equipped with an air brake which was supposed to increase the drag and thus decelerate the car. The concept worked excellently and according to Hawthorn "...he (Fangio) could leave his braking (on the SLR) just about as late as I could on the disc-braked Jaguar..." [1]. Furthermore the air brake seemed to have improved the handling of the SLR. Moss stated that the SLR had "...much better cornering with the air brake in operation" [1]. This, as mentioned earlier, indicates that the air brake increased the car's downforce significantly.

## 1.2 Objective

This project was a direct continuation of the work done by Gullberg and Löfdahl in 2008, with the main purpose to use computational tools to further research the

aerodynamics of the Mercedes-Benz 300 SLR. The aim was to be able to conduct simulations with a higher level of detail and accuracy than those done by Gullberg and Löfdahl. This meant that a higher quality of the computer model of the 300 SLR needed to be made. The aerodynamic performance was then to be analysed by measuring the drag- and lift-coefficients with and without the air brake engaged.

The impact of the air brake was evaluated by comparing the results to aerodynamic data of the SLR from other sources. These were wind tunnel tests carried out in the Daimler-Benz Wind tunnel in Unterturkenheim, Germany aswell as the results presented by Gullberg and Löfdahl.

### 1.3 Delimitations

*Because of the complexity of the problem and time restrictions at hand, some delimitations had to be made. These delimitations and the reason why they were made are listed below.*

Firstly, only steady state simulations was performed. This meant that the SLR's position was held constant during each simulation, as was conditions such as speed and pressures. Also, only straight-on flow was considered, meaning that only the time-averaged velocity field was considered and time varying turbulent fluctuations was ignored.

Secondly, although the CAD model was improved compared to earlier works, it was still a simplified version of the real SLR. Parts which the group considered not to have a significant impact on the aerodynamics of the SLR were neglected altogether. Such parts included for example the hinges connecting the air brake to the car and details in the drivers' area. Some parts were also made with less detail than in real life, such as the wheels which were modelled with flat sides instead of spokes. The reasoning behind this was that adding too much detail would become problematic in the meshing process.

Lastly, thermodynamic effects were neglected. In reality the heat generated by the engine as well as friction heat from the brakes and tyres will to some degree affect the flow. This contribution to the flow was considered to be too insignificant in proportion to the additional work it would take to incorporate it in calculations.



# 2

## Theory of Fluid Mechanics

*In the following section, an overview of the theory used in the project is presented. Firstly, basic theory of fluid mechanics necessary to understand flow properties is explained. This is followed by an introduction to the methods used by CFD software.*

### 2.1 Reynolds transport theorem

A *control volume* is defined as an arbitrarily chosen domain in space which is bounded by imaginary surfaces, hereafter called the *system*. Everything external to this system is referred to as the *surroundings*. The *control surface* is defined as the boundary surfaces between the control volume and the surroundings. Let the letter  $B$  denote any extensive physical quantity of the fluid, for example mass  $m$ , velocity  $\vec{V}$ , angular momentum  $\vec{L}$  or energy  $E$ .

The *Reynolds transport theorem* is a relation between the time derivative of such a system property  $B$  and the rate of change of that same property in a control volume. It reads [5]

$$\frac{d}{dt}(B_{system}) = \frac{d}{dt} \left( \int_{CV} \beta \rho dV \right) + \int_{CS} \beta \rho (\vec{V}_r \cdot \vec{n}) dA, \quad (2.1)$$

where  $\beta := \frac{dB}{dm}$ ,  $\rho$  is the fluid density,  $\vec{n}$  is the unit outward normal of the control volume and  $\vec{V}_r$  is the relative velocity of the fluid through the control volume. If the control volume is chosen to be stationary then  $\vec{V}_r$  is the same as the velocity of the fluid itself. The first term on the right hand side of equation 2.1 is an accumulative term, which describes the accumulation over time of  $B$  within the control volume. The second term represent the in- and outflow across the control surfaces. This theorem basically states that the change over time of an arbitrary fluid property  $B$  in the system is equivalent to the accumulation within the control volume plus the net-flow across the control surfaces.

### 2.2 Conservation of mass and momentum in a fluid

Conservation of mass is a consequence of the continuity equation, which states that the net change of mass in a system is equal to the inflow of mass minus the outflow

of mass. This is equivalent to the mass of a closed system remaining constant, i.e.  $m_{system} = constant$  or  $\dot{m} = 0$ . If the quantity  $B = m$  in equation (2.1), then  $\beta = \frac{dm}{dm} = 1$  and insertion gives the relation

$$\frac{d}{dt}(m_{system}) = 0 = \frac{d}{dt} \left( \int_{CV} \rho dV \right) + \int_{CS} \rho(\vec{V}_r \cdot \vec{n}) dA \quad (2.2)$$

which is known as the *equation of conservation of mass*. If instead  $B$  is chosen to represent the momentum, so that  $B = m\vec{V}$  then  $\beta = \vec{V}$  and equation (2.1) becomes the *momentum balance* for a control volume,

$$\frac{d}{dt}(m\vec{V})_{sys} = \sum \vec{F}_{sys} = \frac{d}{dt} \int_{CV} \rho\vec{V} dV + \int_{CS} \rho\vec{V}(\vec{V}_r \cdot \vec{n}) dA. \quad (2.3)$$

### 2.3 Reynolds number

The Reynold number is the most commonly used quantity which is used to characterise different flow regimes. The Reynold number is defined as

$$Re := \frac{\rho UL}{\mu},$$

where  $U$  is the flow velocity,  $\mu$  is the dynamic viscosity and  $L$  is a characteristic length of the geometry that is being analysed, typically the length or width of a surface. The Reynolds number is a dimensionless quantity that can be interpreted as the ratio between inertial and viscous forces [5].

### 2.4 Compressible and incompressible flow

The flow of a fluid can be classified as either *compressible* or *incompressible*. Saying that a flow is incompressible is equivalent to saying that the density of the flowing fluid is constant in time as well as in space. This means that the continuity equation reduces to,

$$\frac{\partial u_i}{\partial x_i} = \nabla \cdot \mathbf{u} = 0.$$

An easy way to determine if a flow is compressible or not is by calculating the *Mach number*  $Ma$  of the flow. The Mach number is defined as

$$Ma := \frac{u}{a_s}, \quad (2.4)$$

where  $u$  is the local flow velocity and  $a_s$  is the speed of sound in the flowing medium. If  $Ma < 0.3$  the flow can be considered to be incompressible [5].

## 2.5 Bernoulli's Equation

Bernoulli's equation is an idealised energy relation in a fluid. It relates a change the energy of the fluid with reversible pressure work being done between two points in the fluid. In order to be applicable, it is required that the flow is *steady*, *incompressible* and *frictionless*. It is also required that the two points are located along a single streamline. If these requirements are met then Bernoulli's equation reads

$$p_1 + \frac{\rho U_1^2}{2} + \rho g z_1 = p_2 + \frac{\rho U_2^2}{2} + \rho g z_2, \quad (2.5)$$

where  $p_i$  is the fluid pressure at point  $i$ ,  $U_i$  the velocity at point  $i$  and  $z_i$  the vertical position of point  $i$ . The equation can also be restated as

$$\frac{p}{\rho} + \frac{U^2}{2} + gh = \text{constant}. \quad (2.6)$$

The exact value of this constant is often irrelevant, as it is usually the difference in either pressure or velocity between two points that is of interest. In these cases equation (2.5) is often used [6].

A consequence of Bernoulli's equation is that an increase in velocity at a point results in a pressure decrease, and vice versa. This means that the maximum pressure of a fluid is found where the fluid velocity  $V = 0$ . The pressure at such a point is called the *stagnation pressure*.

## 2.6 Aerodynamics

If the velocity on two sides of a body is different, then the pressure will also be different on each side. This creates a pressure gradient over the body, which in turn gives rise to a net force acting on the body and the direction of this force is determined by the direction of the gradient.

If this net force caused by the pressure gradient is directed upwards then it is called a *lift force*  $F_L$ . This is the case when the velocity is higher on the upper side of the body, resulting in a lower pressure there. This is the principle behind so-called airfoils, which purposely increase the flow velocity on the upper side of the foil. If the flow velocity is higher on the bottom side of the body a *downforce*, directed downwards, is generated instead [6].

The *drag force*  $F_D$  on an immersed body arises from two primary sources, pressure gradients and skin friction. Pressure gradients in horizontal directions gives rise to a *pressure drag*  $F_P$ , while friction effects between the fluid and a surface gives rise to *friction drag*  $F_F$ , so that the total drag force can be written  $F_D = F_P + F_F$ . The pressure drag depends on flow separation and the shape of the body, while the friction drag is dependent on the properties of the surface and boundary layer. This means that the friction drag varies greatly with the Reynolds number, which is not the case for pressure drag [7].

### 2.6.1 Drag and lift forces

To calculate the drag and lift forces on an object in a stream there are *coefficients of drag and lift*,  $C_D$  and  $C_L$  respectively, defined as

$$C_D = \frac{F_D}{\frac{1}{2}\rho U^2 A_p} \quad \text{and} \quad C_L = \frac{F_L}{\frac{1}{2}\rho U^2 A_p}. \quad (2.7)$$

In equation (2.7)  $U$  is the free stream velocity and  $A_p$  is a *reference area*, typically the cross-sectional area perpendicular to the stream. Using tabulated values of  $C_D$  and  $C_L$  for simple geometries it is possible to calculate the drag force and lift force of an object through the equations

$$F_D = C_D \left( \frac{1}{2}\rho U^2 A_p \right) \quad \text{and} \quad F_L = C_L \left( \frac{1}{2}\rho U^2 A_p \right). \quad (2.8)$$

### 2.6.2 Laminar and turbulent flow

Apart from attached and separated, flow is classified as being either *laminar* or *turbulent*. The streamlines of laminar flow are moving parallel to one another. The motion of particles is very neat and follows the velocity field precisely. Laminar flow is considered “well behaved” and is characterised by a low Reynolds number.

On the other hand, turbulent flow is characterised by high Reynolds number, generally when  $Re_x > 5 \cdot 10^5$ . The turbulent flow is irregular, usually recirculating and contains quick fluctuations in flow velocity [5].

## 2.7 Navier-Stokes equations

The Navier-Stokes equations are a set of linked, nonlinear partial differential equations which describes flow of Newtonian fluids. Assuming that the flow can be considered incompressible they take the general form

$$\begin{cases} \nabla \cdot \mathbf{u} = 0 \\ \rho \left( \frac{\partial \mathbf{u}}{\partial t} + \mathbf{u} \cdot \nabla \mathbf{u} \right) = -\nabla p - \mu \nabla^2 \mathbf{u} + \rho \mathbf{g} \end{cases} \quad (2.9)$$

where  $\mathbf{u}$  is the flow velocity field,  $\nabla p$  is the pressure gradient and  $\mu$  is the *dynamic viscosity* of the flowing fluid. Given sufficient initial- and boundary conditions these equations fully describe the fluid motion, even if the flow is turbulent. However, it is often not possible to solve them analytically for other than very simple cases. This is the reason why CFD has to be used to obtain numerical approximations of the solutions.

## 2.8 Boundary layer theory

Flow close to surfaces, where friction forces from the surface are considerable, gives rise to a so called *boundary layer* in the fluid. The thickness  $\delta$  of the boundary layer is defined as the distance from the surface to a point where the fluid velocity is 99%

of the free stream velocity. The character and thickness of the boundary layer is strongly dependent on the corresponding Reynolds number.

In a turbulent flow, the boundary layer is generally divided into three regions,

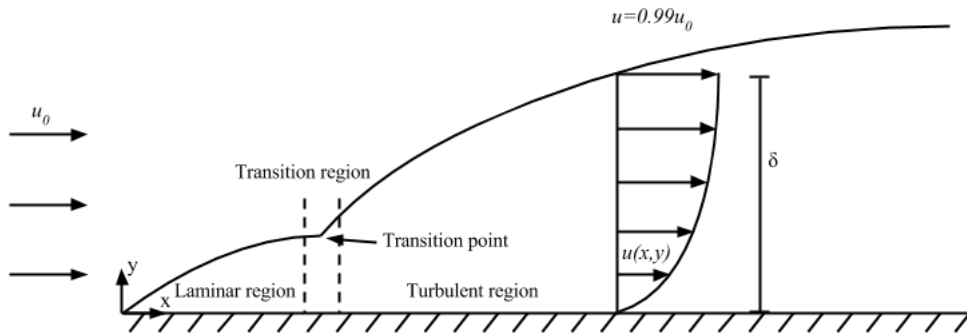


**Figure 2.1:** A schematic boundary layer velocity profile. A uniform free stream with velocity  $u_0$  approaches a flat plate in the  $x$ -direction. A laminar boundary layer starts to form immediately over the plate. As the fluid travels further across the plate the laminar boundary layer thickens, until it reaches a transition point where the flow becomes increasingly turbulent.

- The wall region, where viscous forces are dominant
- An outer region, where turbulent stresses are dominant
- An overlap layer connecting the other two.

A typical boundary layer velocity profile can be seen in figure 2.1.

### 2.8.1 Attached and separated flow

Flow past an immersed body can be classified as either *attached* or *separated*. If the streamlines of the flow follow the shape of the body the flow is said to be attached, while if this is not the case the flow is instead said to be separated from the body surface [6]. Separation is caused by an *adverse pressure gradient*, i.e. an increase of pressure along the stream direction. Separated flow behind a body is usually undesired, as it results in a backflow in the stream. Such backflow gives rise to a *wake*, which is a region where the flow is irregular and often turbulent. This creates vortex shedding, increasing energy loss due to an increase of momentum transfer in the recirculating fluid.

## 2.9 Turbulence modelling

Due to the complex nature of turbulence, several methods of modelling have been developed. The choice of model depends primarily on the geometry of the analysed

system and what kind of information is sought. A common trait amongst the different methods is that they utilise some sort of averaging to simplify the turbulent velocity field.

### 2.9.1 Reynolds Averaged Navier-Stokes

A simple model of a turbulent velocity field  $\mathbf{u}$  is to decompose it into a sum of a fluctuating part  $\mathbf{u}'$  and an time-averaged part  $\bar{\mathbf{u}}$ , so that

$$\mathbf{u}(x, y, z, t) = \mathbf{u}'(x, y, z, t) + \bar{\mathbf{u}}(x, y, z, t),$$

a procedure known as Reynolds decomposition. Insertion into the Navier-Stokes equations (2.9) gives the Reynolds Averaged Navier-Stokes, or *RANS*, equations,

$$\rho \left( \frac{\partial \bar{u}_j \bar{u}_i}{\partial x_j} \right) = \rho \bar{f}_i + \frac{\partial}{\partial x_j} \left( -\bar{p} \delta_{ij} + \mu \left( \frac{\partial \bar{u}_i}{\partial x_j} + \frac{\partial \bar{u}_j}{\partial x_i} \right) - \overline{\rho u'_i u'_j} \right). \quad (2.10)$$

This equation is similar to the ordinary Navier-Stokes equation except that the time-averaged fields  $\bar{\mathbf{u}}$  and  $\bar{p}$  are used rather than the ordinary velocity and pressure fields. The last term,  $-\overline{\rho u'_i u'_j}$  is known as the *Reynolds stress* and is modelled differently depending on the chosen turbulence model.

### 2.9.2 Realizable k- $\epsilon$ model

A recent, commonly used turbulence model based on the RANS-equations is the *realizable k- $\epsilon$  model*. This model makes use of the Boussinesq-assumption to model the Reynold stress. With this model the Reynolds stress is calculated using

$$\overline{\rho u'_i u'_j} = 2\mu_t S_{ij} - \frac{2}{3}\rho k \delta_{ij}, \quad (2.11)$$

where  $\mu_t$  is the *eddy viscosity* of the mean flow,

$$S_{ij} = \frac{1}{2} \left( \frac{\partial u_i}{\partial x_j} + \frac{\partial u_j}{\partial x_i} \right) \quad (2.12)$$

is the mean flow strain rate, recognised from the RANS-equations,  $k$  is the turbulent kinetic energy and  $\delta_{ij}$  is the Kronecker delta. The turbulent eddy viscosity  $\mu_t$  is in turn determined by both the turbulent energy  $k$  and the energy dissipation factor  $\epsilon$ ,

$$\mu_t = \rho C_\mu \frac{k^2}{\epsilon}.$$

The constant  $C_\mu$  is a dimensionless structure factor, whose exact value depends on the strain tensor  $S_{ij}$  through the expression

$$C_\mu = \frac{1}{A_0 + A_s \frac{kU_*}{\epsilon}},$$

where  $A_0$  is a model constant and  $A_s$  is a flow dependent variable. Details of the exact definition of all model parameters can be found at [8]. Introducing this model, two extra transport equations for  $k$  and  $\epsilon$  has to be solved. This results in a computationally heavy method, but with better performance than other turbulence models for many types of flows [9].

### 2.9.3 Modelling of porous media

For flow through a porous medium, such as a sand bank or radiator, an increase in flow resistance causes a corresponding pressure drop through the medium. Instead of attempting to resolve the flow through such a complex interface it is possible to model a pressure drop across the interface. An empirical model of the pressure drop is [10]

$$-\nabla p = \alpha\mu\mathbf{u} + \rho\beta_I\mathbf{u}^2, \quad (2.13)$$

where  $\alpha$  is the viscous resistance term and  $\beta_I$  is the inertial resistance term, both are which are dependent on specific properties of the porous medium.

### 2.9.4 Wall treatment

In order to simplify simulations and reduce computing time, the regions closest to bodies and walls are usually not resolved using a turbulence model, but rather by using a *wall treatment* approximation. An approximation that is valid for the outer layer described earlier is the *logarithmic wall law*. The approximation introduces the dimensionless velocity  $u^+$  and distance  $y^+$ , defined as

$$u^+ = \frac{u}{u^*} = \frac{1}{\kappa}\ln(y^+) + A \quad \text{and} \quad y^+ = \frac{yu^*}{\nu},$$

where  $u^*$  is the friction velocity which is in turn defined as

$$u^* = \sqrt{\frac{\tau_w}{\rho}},$$

where  $\tau_w$  is the wall shear stress. A common approximation in the outer layer is to use the velocity profile

$$u^+ = 2.44\ln(y^+) + 5, \quad (2.14)$$

which is valid in the region  $30 < y^+ < 300$ .

In the viscous sublayer closest to the wall, when  $y^+ < 5$ , the velocity profile can be approximated as

$$u^+ = y^+,$$

while in the buffer layer between  $5 < y^+ < 30$  neither of the previous approximations are valid. However, the region where  $y^+ < 30$  constitutes only a very small part of the total boundary layer, and the velocity profile further out varies very little from the logarithmic law. The logarithmic law is therefore often used to approximate the velocity profile across the entire boundary region without too much loss of accuracy [11].

## 2.10 The Finite Volume Method

The finite volume method, or *FVM* for short, is a way of solving differential equations and is commonly used in numerical fluid dynamic calculations. The idea of the method is to divide the region in which the flow is to be analysed into discrete

control volumes and then numerically solve the integral conservation laws (2.2) and (2.3) governing the flow in each of these volumes.

The discrete solution in each of these volumes is then interpolated to those in surrounding cells in an iterative process, which is repeated until the residual errors of the solutions converge. This process results in a solution to the original differential equations for the entire domain.

# 3

## Method

*This section outlines the methods that were used to finish the thesis. In order to provide a framework for the project, work progress was structured around three major phases which are outlined below.*

- *Pre-processing using CATIA and ANSA*
  - Transferring the laser-scanned model of the 300SLR to CATIA
  - CAD-modelling of the 300SLR in CATIA
  - Cleaning and creating a surface mesh using ANSA
- *Simulations in STAR CCM+*
  - Selection of suitable parameters for simulations
  - CFD solutions using STAR CCM+
- *Post-processing and analysis*
  - Visualisation of results
  - Interpretation and analysis of CFD calculations

### 3.1 Pre-processing

The main purpose of the pre-processing part was to create a good basis for future meshing and CFD simulations. The basis for the CAD-work consisted of a laser scanned model of the car body. The laser-scan was presented as a cloud of points in three dimensional space and a new surface was required to be constructed. Although the scanning was made by an advanced and modern scanner some of the smaller details were ignored or poorly scanned and were needed to be created and added to the car manually instead. Most of the work was done using the CAD-software *CATIA* and the pre-processor software *ANSA*.

#### 3.1.1 Preparing the laser-scan

The starting point for the project was the surface model of the Mercedes Benz 300 SLR used by Löfdahl and Gullberg. This model originates from a laser-scan of a 1:24



**Figure 3.1:** Die-cast 1:24 Fangio/Moss Mercedes 300 SLR. From [1], reproduced with permission.

die-cast model of the car.[1] The die-cast model can be seen in figure 3.1. The surface model used by Löfdahl and Gullberg was presented in a format which could not be directly imported into CATIA. In order to use the data in CATIA the model was first imported into ANSA. The outline of the car was extracted by making vertical cross-section cuts along several planes perpendicular to the car. This resulted in “slices” of the car, as can be seen in figure 3.2. The cross-sectional planes were made closer than necessary in order to make it possible to choose the most suitable planes for recreating the body. A similar process was also utilised to recreate the cars’ air brake.

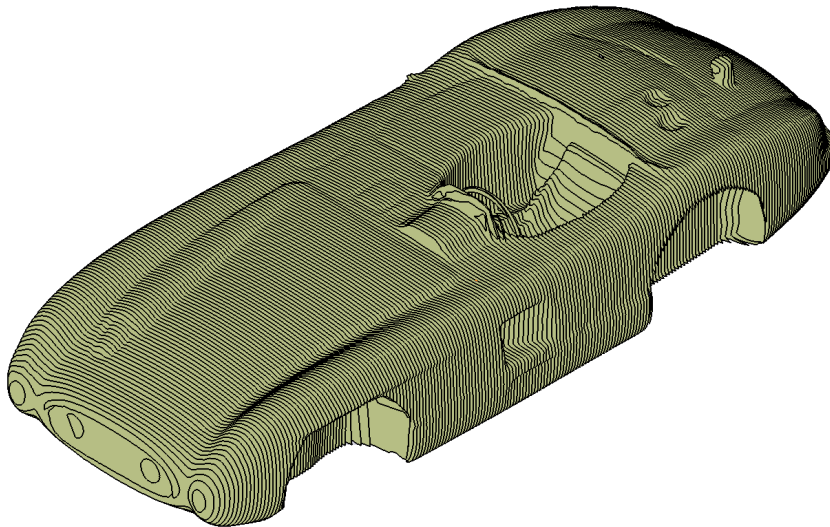


**Figure 3.2:** The result of extracting contour-curves from the laser scanned model of the Mercedes.

#### 3.1.2 Modelling of the car body and air brake

Once the entire car and air brake had been sliced up into cross-section segments, the slices were imported into CATIA. In order to achieve a smooth body surface a

copy of each slice's border was made. These outlines were then traced using splines in order to get smooth curves along the entire body. Additional splines were then created along the length of the car to act as guides for the creation of the surface. This had to be done for the program not to compromise on the edges. The final model surface was then made as a swept body along the splines and guides using the function "*Multi-section surface*" in CATIA. The result is seen in figure 3.3.

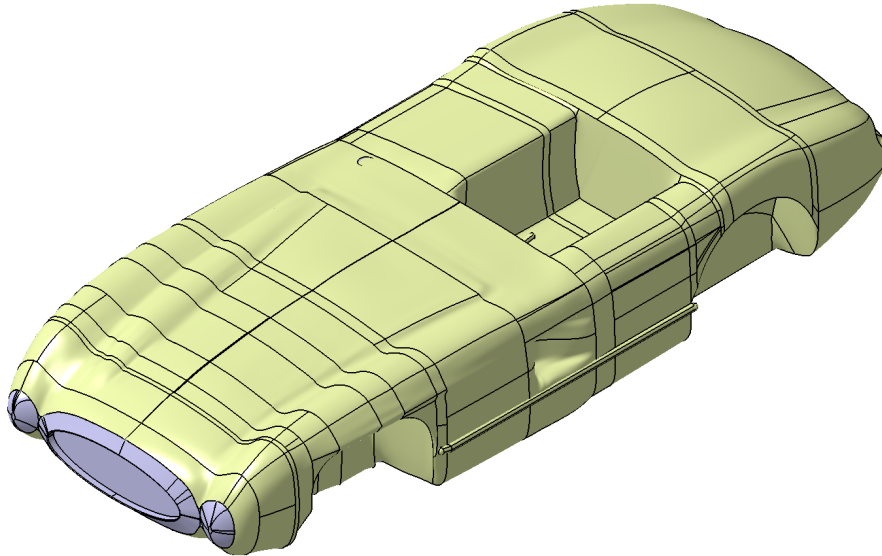


**Figure 3.3:** The reconstructed car body before cleaning and finishing work had been done. The black lines are the splines and guidelines that were used to create this surface.

### 3.1.3 Modelling of exterior parts

To improve the accuracy of future CFD-calculations, certain smaller details of the car were remodelled. The parts chosen to be included were selected by considering their possible impact on flow patterns. The parts included were

- Wheels
- Windshield
- Rear-view mirror
- Steering wheel
- Seat
- Exhaust pipes
- Headlights

The wheels were modelled according to the specifications found on a website called "automobile catalog" [4], and are recited in table 3.1. The wheelbase was set to 2370 mm and the front and rear track to 1330 mm and 1380 mm respectively, according to data on this website. The other parts were recreated from the die-cast model using callipers and eye measure and then scaled 24 times. All external CAD-parts can be found in appendix A, CAD models.

**Table 3.1:** Wheel dimensions - Mercedes-Benz 300 SLR.

Tyres	Rim size (in)	Total wheel diameter (mm)	Tyre width (mm)
Rear	16	727	178
Front	16	727 <sup>1</sup>	152.4

<sup>1</sup> According to automobile catalog this figure only applies to the rear wheels. It was assumed, however, that since the wheels had the same rim, they probably had approximately the same diameter.

### 3.1.4 Modelling the internal parts

Contrary to Gullberg and Löfdahl, who had used a completely closed model, a simulation with airflow through the car's interior was planned. This meant that the internal parts of the SLR had to be modelled. Due to lack of CAD-basis and

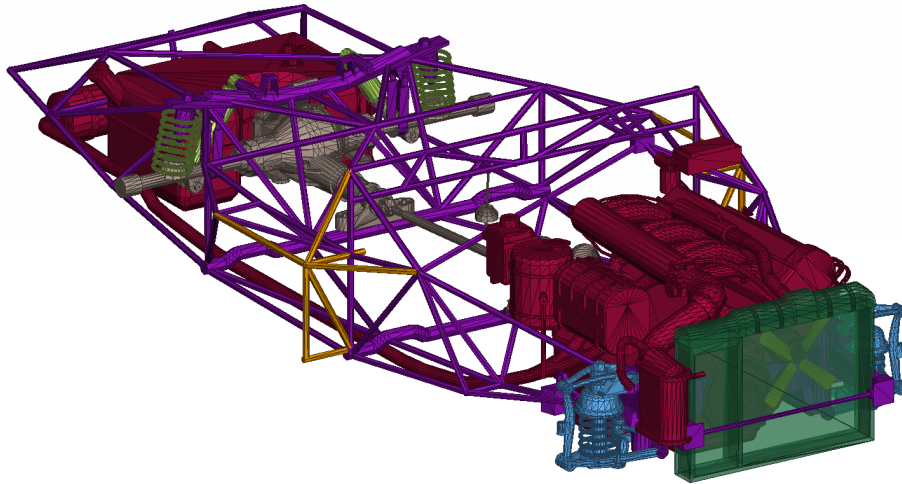


**Figure 3.4:** The internal parts of the Mercedes 300 SL. Included is the chassis, radiator, engine, transmission, fuel tank and suspension. The blades of the radiator fan and part of the chassis (yellow) were excluded.

limited time, these parts were imported from a CAD-model of the similar Mercedes-Benz 300 SL<sup>1</sup>. The SL's powertrain and chassis were deemed to give a fairly good representation of the SLR's interior. However, there were some important differences between the two cars. The most obvious one is that the SL's chassis was slightly wider than the body of the SLR. To fit properly, some parts of the chassis structure were removed to prevent them from protruding through the car body, see figure 3.4. Also the SL's engine, a slightly smaller 3 litre straight 6, had to be lowered 2.5 cm to fit under the SLR's bonnet. Furthermore, all the extra fuel tanks needed for the 24-hour race were missing in the SL. All work with fitting the interior parts was done in ANSA. The result is found in figure 3.4.

<sup>1</sup>The model was bought and downloaded from <http://www.3dcadbrowser.com/download.aspx?3dmodel=5514>

### 3.1.5 Merging the model

Once the body, air brake and exterior parts of the car had been modelled and a satisfactory level of detail had been obtained, the CAD-model was imported into ANSA. The model was then cleaned using ANSA’s functions to patch holes, remove overlapping surfaces and making sure that surfaces and bodies were properly connected.

When the CAD-model had been cleaned, it was merged with the internal parts of the SL. Here a previously neglected problem occurred, namely the scaling of the SL. In spite of thorough search no record of the SL’s scale was found, and so the internal parts were simply scaled so as to fit the SL’s suspension to the SLR’s wheelbase. As mentioned earlier, this meant that part of the chassis had to be removed. The ground clearance was modified to match the specifications [12]. Even with the powertrain, chassis and fuel tank from the SL, the interior of the car was deemed to be unrealistically empty. To address this, a cockpit was created to fill some of the empty space in the cars interior.

A driver, in the form of a manikin from the CATIA “Human builder” library, was also imported and added into the cockpit. For added realism the driver was equipped with a helmet, which was created in CATIA. Both the driver and helmet models can be found in appendix A, CAD models.

Lastly, the virtual wind tunnel was created in ANSA. It was made as a rectangular tunnel, which extended five car-lengths upstream and 10 car-lengths downstream. The cross section was five car-lengths wide and 2.5 car-lengths high. These dimensions were chosen in accordance to the recommendations in the tutorials on external aerodynamic simulations in ANSA [13]. With all parts in place, the model was

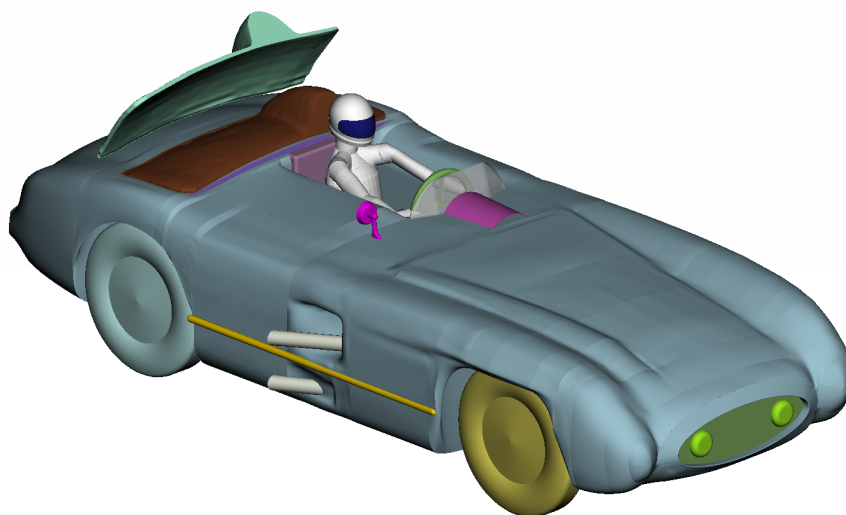


**Figure 3.5:** Final model of the Mercedes-Benz 300 SLR. Different colours represent different PID’s. Note that the air brake is shown both in high and low position.

organised by assigning so called PID’s, short for Property ID’s, to different parts of the car and wind tunnel. The purpose of this was twofold. Firstly, it enabled

modifications of individual parts separately from the rest of the model. For example, the air brake could easily be tilted between positions. Secondly, the splitting of the model into different PID's is transferred to STAR CCM+ and thus makes it possible to assign different mesh- or physics settings or different boundary conditions to different PID's. The final model can be seen in figure 3.5, and a complete list of all PID's can be found in appendix B, PID's.

To get a more realistic interior airflow in the model with open cooling it was required to force air through the radiator. The area between the car body and radiator was therefore sealed in order to force the air coming in through the front-grille through the radiator which can be seen in figure 3.6.

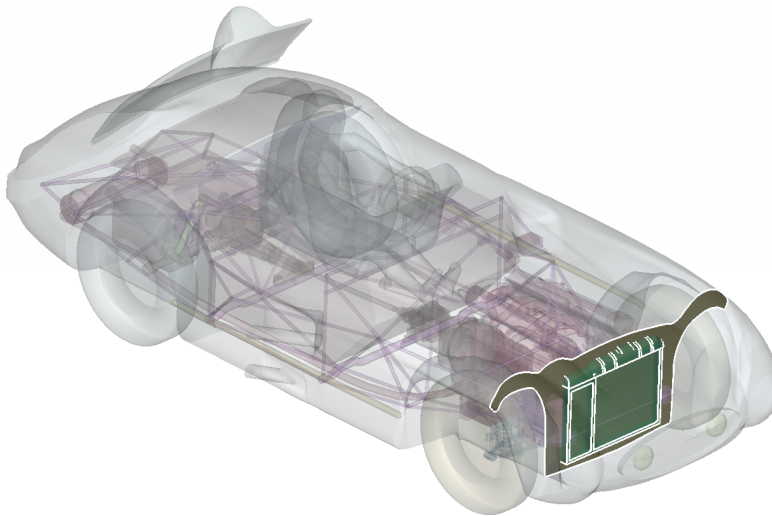


**Figure 3.6:** An illustration of the plane intended to force the incoming air through the radiator.

#### 3.1.6 Surface wrapping and meshing

The finished files were exported from ANSA and imported to the CFD software STAR CCM+, where the simulations would be made. In total, four different models were exported. Closed and open body, both with the air brake positioned up and down. However, before any simulations could be run additional setup and preparation work had to be done. This process included

- Creating a surface wrap to obtain a base surface
- Creating a new surface mesh
- Extending the surface mesh to a volume mesh of the entire fluid domain
- Defining boundary conditions for all surfaces
- Defining physics settings for the flow

The surface wrap was needed to get a representation of the surface which was suitable for future simulations, as the file imported from ANSA contained errors which made it unsuitable for CFD-simulations. Settings for the surface wrap can be found in table 3.2. Additional contact prevention constraints were added in relevant areas to

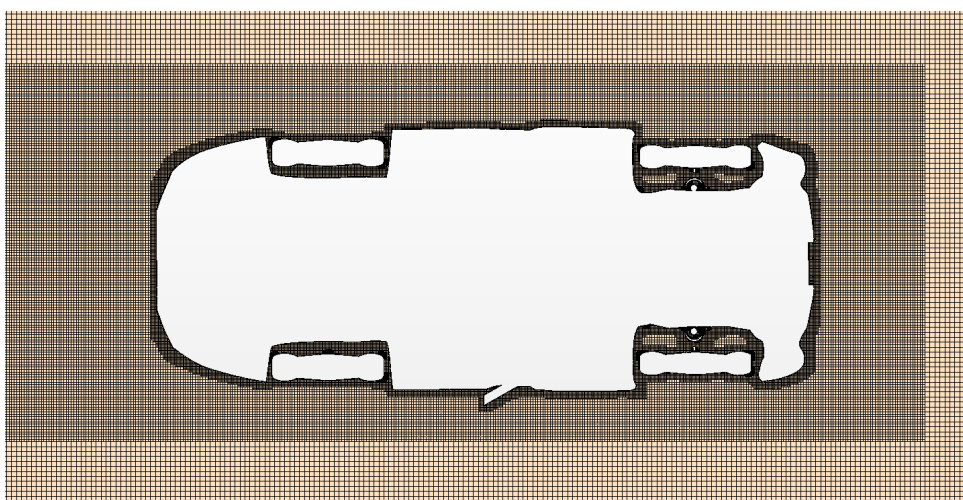
**Table 3.2:** Settings used for the surface wrap and later for the surface mesh.

Base size	8 mm
Target surface size	8 mm
Minimum surface size	4 mm
Surface curvature	60 pts/circle

prevent the surface wrapper from joining separate parts together. With a completed surface wrap in place a new surface mesh was created using the same settings. When creating the volume mesh, the mesh cell sizes were based on how accurately the flow needed to be simulated around different parts. Refinement boxes, where a smaller target cell size was specified, were added in regions of interest such as above the driver and in the wake behind the car. The settings used for the volume mesh can be found in table 3.3. Cross-sectional cuts of the volume mesh can be seen in figures 3.7 and 3.8, where features such as refinement boxes and prism layers can be seen.

**Table 3.3:** Settings used for the volume mesh. Refinement boxes, specifying a finer cell size, were used to increase resolution in volumes of interest around the car.

Mesh type	Trimmed cell mesher Prism layer mesher
Base size	8.0 mm
Target surface size	8.0 mm
Minimum surface size	4.0 mm
Maximum cell size	256.0 mm
Number of prism layers	2
Prism layer stretching	1.5
Prism layer thickness	33% of base size

**Figure 3.7:** A horizontal cross section of the volume mesh. A higher cell density can be seen in darker areas around the car body, while the mesh is sparser further away.

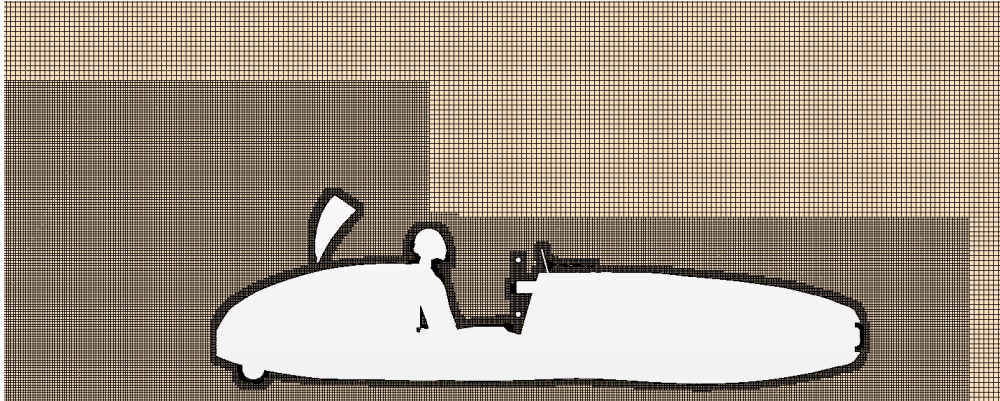


**Figure 3.8:** A vertical cross section of the volume mesh. As in figure 3.7 the mesh can be seen to be denser around wheels, while it is sparser further away from the car. The dark region closest to the car is the prism layers used to simulate the boundary layer.

## 3.2 CFD simulations

*The completion of the project depended on obtaining good results from CFD simulations of the flow around the 300SLR. This section presents how these simulations were made.*

The simulations were intended to recreate conditions corresponding to the 300SLR travelling straight forward. Simulations were also made with closed and open cooling, where the closed cooling simulations were primarily meant to be used for comparison, whereas open cooling was meant to give simulations that were more realistic. To evaluate the effects of different speed, simulations were also made with the open model of the car travelling at 120 and 180 kph. The final simulations that were made were

- Closed cooling
  - air brake up, 120 kph
  - air brake down, 120 kph
- Open cooling
  - air brake up, 120 and 180 kph
  - air brake down, 120 and 180 kph

### 3.2.1 Boundary conditions

In order to make simulations converge to give good results, proper boundary conditions had to be set on each surface. Most stationary parts were simply identified as stationary walls with a no-slip condition. Wheels were set as moving walls, rotating with a constant angular velocity around an axis placed through each wheel axis. To simulate the car moving forward the ground was set as wall moving with the same

speed at which the car is moving. In the cases where the simulations were run with an open cooling the radiator was set as a porous medium to mimic a pressure drop across the air intake. The values for the porous conditions were based on previous years work [14]. The specific settings for all boundary conditions are found in table 3.4.

**Table 3.4:** Boundary conditions for surfaces which were not considered stationary walls. The radiator conditions were only applied in simulations with open cooling, while the rest were used in all simulations.

Part	Boundary condition	Values
Wheels	Wall relative rotation	<i>Angular velocity:</i> 91.7 rad/s / 137.6 rad/s
Radiator	Porous medium	<i>Porous inertial resistance:</i> $XX = 900 \text{ kg/m}^4$ $YY = 90000 \text{ kg/m}^4$ $ZZ = 90000 \text{ kg/m}^4$  <i>Porous viscous resistance:</i> $XX = 450 \text{ kg/m}^3 \cdot \text{s}$ $YY = 45000 \text{ kg/m}^3 \cdot \text{s}$ $ZZ = 45000 \text{ kg/m}^3 \cdot \text{s}$
Ground	Moving wall	<i>Velocity:</i> 120 kph / 180 kph
Walls, roof	Symmetry plane	N/A
Inlet	Velocity inlet	<i>Velocity:</i> 120 kph / 180 kph <i>Turbulent viscosity ratio:</i> 1 <i>Turbulent intensity:</i> 0.01
Outlet	Pressure outlet	<i>Constant pressure:</i> 0 Pa <i>Turbulent viscosity ratio:</i> 1 <i>Turbulent intensity:</i> 0.01

### 3.2.2 Physics settings

In addition to correct boundary conditions, proper settings for the physics models used by the solver was required in order for simulations to be representative of real world conditions. These settings can be found in table 3.5.

## 3.3 Post-processing

Most post-process analyses were made using the *monitors* from STAR CCM+. By selecting proper variables to monitor the software directly gave numerical values presented *reports* after each simulation. Particular variables on interest to monitor were obviously the drag and lift coefficients, and by also monitoring the momentum of the car it was possible to calculate the corresponding lift and drag forces. The pressure field around the car was also monitored in order to determine where the flow separated from the surfaces of the car.

**Table 3.5:** Physics settings used by the solver during simulations.

Cell quality remediation
Constant density
Coupled flow
Steady flow
Three dimensional flow
Turbulent flow
Reynolds Averages Navier-Stokes
k- $\epsilon$ turbulence
Realizable k- $\epsilon$ two-layer
Two-layer all $y^+$ wall treatment

In order to visualise the data, *scenes* were used. These allowed graphical visualisation of velocity fields, pressure fields and areas of flow separation around the car which simplified further analysis. The use of scenes to visualise the flow also made it possible to judge the quality of a simulation by looking for unreasonable flow patterns, preventing unnecessary analysis of unphysical results.

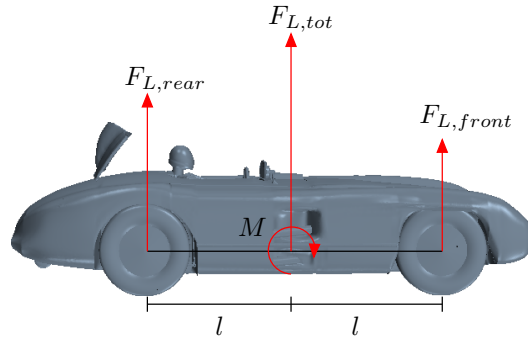


**Figure 3.9:** Force distribution over the car.

Given the total lift force  $F_{L,tot}$  and the momentum  $M$  defined according to figure 3.9 above, the force distribution on the wheel axis was calculated as follows. Replacing the total lift force with two new forces  $F_{L,rear}$  and  $F_{L,front}$  as in the sketch we get

$$F_{L,tot} = F_{L,rear} + F_{L,front} \quad (3.1)$$

and

$$M = lF_{L,rear} - lF_{L,front}. \quad (3.2)$$

Equations (3.1) and (3.2) form a system of linear equations with two unknowns. Solving the system yields

$$\begin{cases} F_{L,rear} = \frac{F_{L,tot}}{2} + \frac{M}{2l} \\ F_{L,front} = \frac{F_{L,tot}}{2} - \frac{M}{2l} \end{cases}$$

which is the desired relation.

# 4

## Results of CFD simulations

*In this section the results of CFD simulations in STAR CCM+ is presented. Only the direct results are show, as further analysis of them are presented in the Discussion and Analysis chapter of the report.*

Simulations were run at 120 kph with the cooling of the Mercedes both closed and open. Only the model with open cooling was simulated at the velocity of 180 kph. The coefficients of drag and lift as well as the corresponding *total* drag and lift forces were calculated using reports in STAR CCM+. For these calculations a reference area  $A_p = 1.4545 \text{ m}^2$  was used. This is the cross-sectional area of the SLR with the air brake down, perpendicular to the stream.

### 4.1 Closed cooling

**Table 4.1:** Calculated values for the drag and lift coefficients  $C_D$  and  $C_L$ , as well as the drag and lift forces  $F_D$  and  $F_L$  for the closed model at 120 kph. Positive values indicates a lift force directed upwards.

Air brake	Velocity	$C_D$	$F_D$	M	$C_L$	$F_L$ (Front)	$F_L$ (Rear)
Down	120 kph	0.273	261 N	29 Nm	0.257	111 N	135 N
Engaged	120 kph	0.708	677 N	-441 Nm	-0.119	129 N	-243 N

The open cooling simulations show a significant increase of the drag with the air brake in operation. As can be seen in figure 4.1 a large low-pressure wake is created behind the 300 SLR when the air brake is engaged. A decrease in the lift coefficient also arises when the air brake is engaged. The lift force distribution is also seen to change between the two positions. With the air brake in the downright position the downforce is almost evenly distributed, with only a slightly higher lift on the rear wheels. However, when the air brake is engaged a large downforce is generated on the rear, with only a small increase in front axis lift force, implying an increased total downforce.

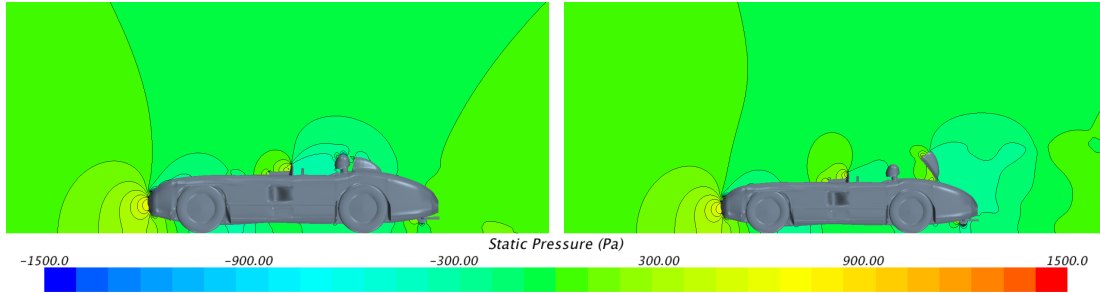


**Figure 4.1:** Scalar field of the static pressure around the open model of the SLR at 120 kph.

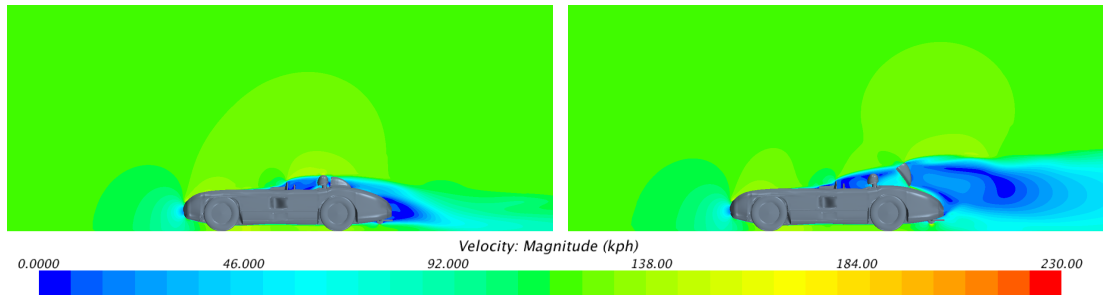


**Figure 4.2:** Scalar field of the velocity magnitude around the closed model of the SLR at 120 kph. Stagnation can be observed in front of the driver as well as in a small wake behind the car. A larger wake of stagnation can be seen behind the car with the air brake engaged. The flow velocity around the driver is also lower in a larger volume than when the air brake is down.

## 4.2 Open cooling

**Table 4.2:** Calculated values for the drag and lift coefficients  $C_D$  and  $C_L$ , as well as the drag and lift forces  $F_D$  and  $F_L$  for the open model at different speeds. Positive values indicates a lift force directed upwards.

Air brake	Velocity	$C_D$	$F_D$	M	$C_L$	$F_L$ (Front)	$F_L$ (Rear)
Down	120 kph	0.150	143 N	-22 Nm	0.380	191 N	173 N
	180 kph	0.163	351 N	-41 Nm	0.391	438 N	403 N
Engaged	120 kph	0.556	532 N	-459 Nm	-0.026	181 N	-206 N
	180 kph	0.563	1213 N	-1033 Nm	-0.023	411 N	-461 N

As for the case with the closed cooling simulations the air brake results in a significant drag force increase as well as a redistribution of the lift force on each wheel axis. The open cooling also gives rise to smaller values for  $C_D$ , while  $C_L$  increases compared to the closed cooling. This results in a smaller drag force and an increased lift force than with the closed cooling model.

The airflow through the radiator resulted in a pressure drop across the radiator interface. The pressure drop value, as well as the mass flow through the radiator, can be found in table 4.3. The pressure field around the radiator can be seen in

**Table 4.3:** Pressure drop across, and mass flow through the radiator for both 120 and 180 kph.

Velocity	Pressure drop [Pa]	Mass flow [kg/s]	Area [m <sup>2</sup> ]
120 kph	744	0.72	0.183
180 kph	1723	1.12	0.183

figure 4.3. The resulting airflow through the radiator and undercarriage, in the form of streamlines, at 120 kph can also be seen in figure 4.4.

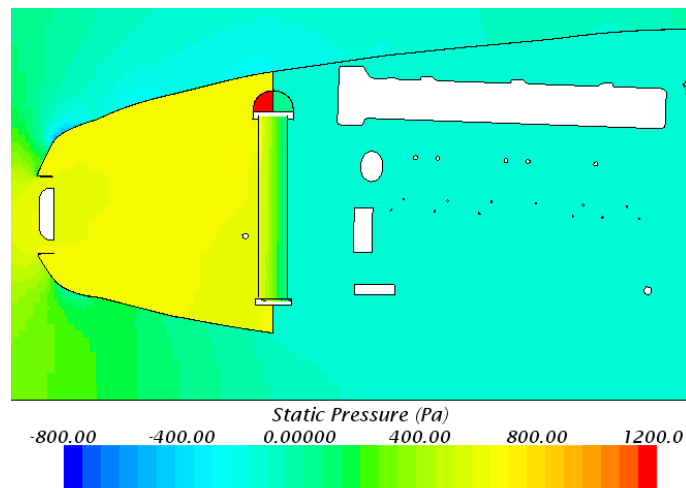


**Figure 4.3:** Static pressure around the radiator viewed from a cut through the middle of the car in the direction of travel.

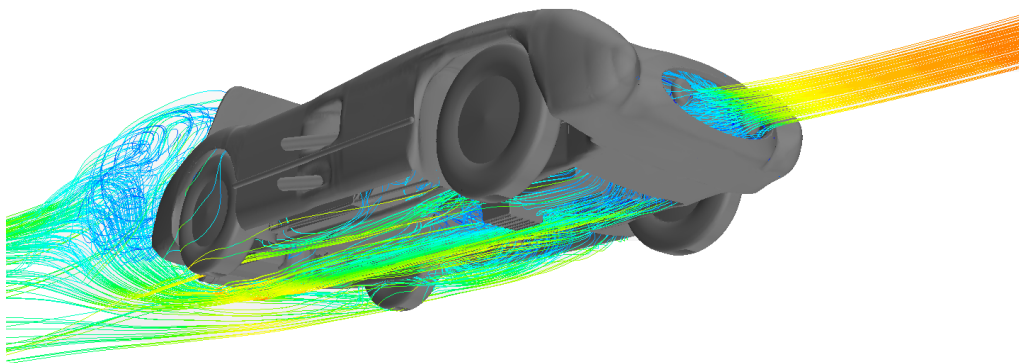


**Figure 4.4:** Streamlines of the airflow through the radiator and interior of the car.

#### 4. Results of CFD simulations

---

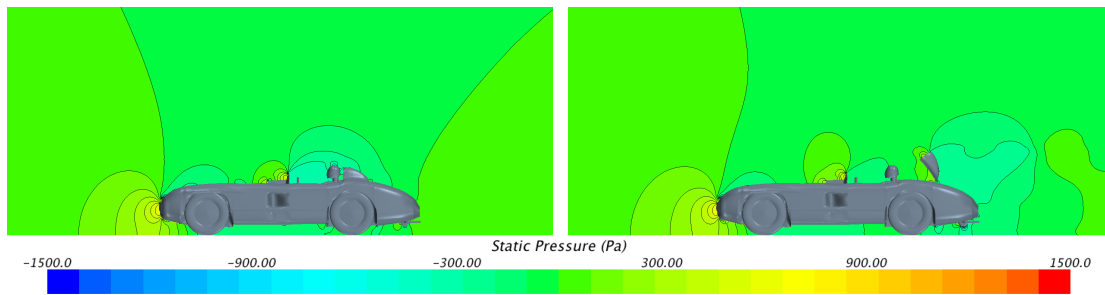


**Figure 4.5:** Scalar field of the static pressure around the open model of the SLR at 120 kph.

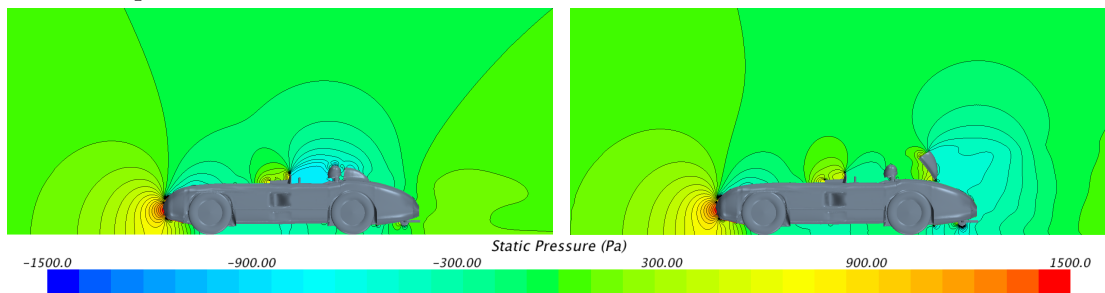


**Figure 4.6:** Scalar field of the static pressure around the open model of the SLR at 180 kph.

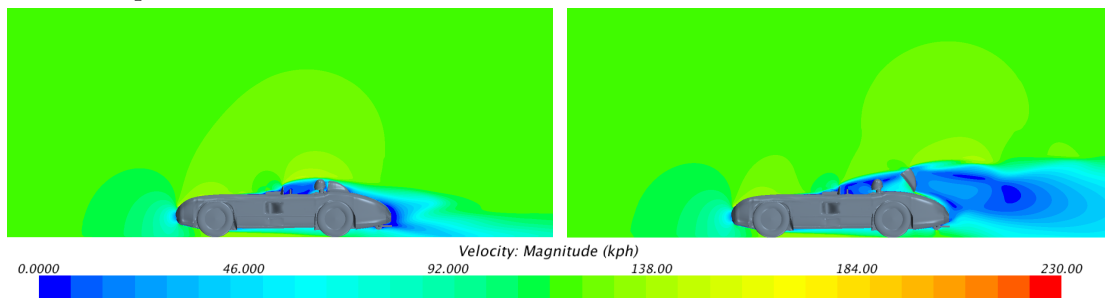


**Figure 4.7:** Scalar field of the velocity magnitude around the open model of the SLR at 120 kph.

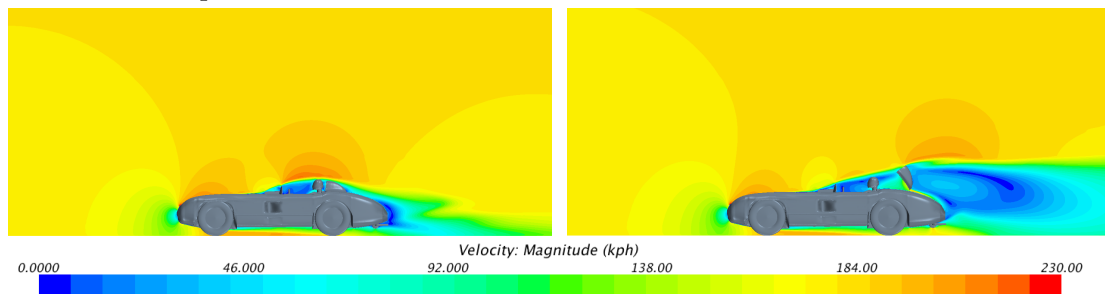


**Figure 4.8:** Scalar field of the velocity magnitude around the open model of the SLR at 180 kph.

# 5

## Discussion and Analysis

*In this section the results and the methods used to achieve them, will be discussed. A comparison with earlier, similar works will also be done.*

The simulations done in this report were of the most common type of CFD with no tilt nor pitch. The setup of the simulations were of the easier nature but provides valuable information and results for conclusions to be made. This report chooses to focus on the drag and lift forces, which are results of pressure difference between the front and rear of the car respective lower and upper half of the car.

### 5.1 Comments on methodology

*This section aims to give a motivation to the choices of methods used during the project. Possible disadvantages with these methods are also discussed.*

The methodology used in this project was a fairly standardised method for CFD. The overall process of first creating a CAD model, meshing it and then exporting the mesh into CFD-software for flow analysis could most likely not have been done in any other way. The individual stages of the work process, however, could have been done in a multitude of ways. The choices of method in this project was mostly based on previous years work on similar CFD-simulations.

#### 5.1.1 Pre processing

The main purpose of this project was to do CFD simulations on the same Mercedes 300 SLR that was used in the Le Mans Race of 1955. The model was acquired through “pointcloud” data, which was not directly useable for simulations. When searching for methods to make the data suitable for CFD a software which could convert the data into a CAD model was found. However, this software was not offered by Chalmers University. Instead the method of using splines in CATIA, inspired from last years work [14], was chosen. With free online tutorials to complement for inadequate knowledge, a better model was created. Although a large amount of cross-sectional slices was originally made, it was concluded that a smoother surface could be obtained by using fewer slices and guide curves for the car shape, as discussed in Modelling of the car body and air brake. This resulted in fewer sharp edges at the connections between surfaces of the car, and in turn a smoother finish to the entire surface.

The undercarriage that was purchased for the car was attached to the model through the software ANSA before exporting it to STAR CCM+ to perform the volume mesh and simulations. ANSA was the only software offered that could open and process the type of file extensions that the undercarriage was saved in. To effectively use ANSA, studies of the tutorials supplied with the program had to be undertaken. STAR CCM+ was a complicated software, as it offered more detailed settings on the simulations that could be adjusted in comparison to other CFD-software on the market. This meant that it took longer time to get simulations running than it would have with other, simpler CFD-software.

### 5.1.2 Solving

As mentioned earlier, STAR CCM+ was regarded a complicated software which led to several hours spent consulting with the supervisors. A majority of the settings in the first simulations were recommended by the supervisors. These were then tweaked as better knowledge of the software was gained, in order to obtain better results. The first simulation took nearly two full weeks but as soon as the user became more familiarised with the software the simulation time decreased, around one day per simulation. Due to problems with convergence of the simulations, some solutions were obtained with residuals from the finished simulation being higher than optimal. This in turn meant that the results from simulations were not as good as they could be. Time restraints unfortunately meant that not enough time could be put into further minimising residuals.

### 5.1.3 Post processing

All used data were acquired from STAR CCM+. Some solutions also tended to oscillate even though the residuals were low. To get values from these simulations the measured values were averaged over the iterations where oscillation occurred. The oscillations were so small that the induced error was small enough that the averaged results was considered valid.

## 5.2 Drag forces

When the air brake is engaged a large drag is generated on the Mercedes, which from its intended function could be expected. The closed model had a higher drag coefficient than the open model, both with and without the air brake engaged as can be seen in tables 4.1 and 4.2. The closed model also showed a larger difference in drag coefficient between air brake positions than the open model.

The drag coefficient of 0.273 for the closed model without the air brake engaged is quite low, and is comparable to the drag coefficient of many modern cars. On the other hand, the drag coefficient of the open model at the same speed is only 0.15 which is incredibly low. Such a drag coefficient is only matched by modern experimental vehicles where uttermost care has been taken to optimise aerodynamic performance.

Comparing the effect of velocity on the drag, as can be seen in table 4.2, increased speed slightly increases the drag coefficient, which could be a consequence of the simulations not converging enough. From equation 2.8 it is known that the drag force is not only proportional to the drag coefficient, but also to the velocity squared. The velocity increase of the car thus results in a large increase in drag. This means that the air brake would be especially efficient at increasing the braking ability of the 300 SLR at high speeds.

### 5.3 Lift force

As mentioned in chapter 2, a lift or downforce arises from a pressure difference between the upper and lower side of the cars' body. Figure 4.1 shows that the overall pressure along the top of the car is lower than beneath it. When the air brake is not engaged, this results in a aerodynamic lift that is slightly larger on the front axis than on the rear axis. This force distribution was present in all simulations and can be seen in tables 4.1 and 4.2.

However, when the air brake is engaged the car no longer experiences a total lift force. The aerodynamic lift on the front wheels is roughly unchanged, with only a small increase in lift with closed cooling and a slight decrease with open cooling. The rear wheels instead experiences a large downforce. When the air brake is engaged, simulations show a large, clockwise moment generated around the centre of the car. This moment seeks to lift the front axis and press the rear axis downwards. The downforce on the rear axis is so large that the total aerodynamic lift on the Mercedes is directed downwards, so that the car overall experiences a downforce.

An overall downforce implies better handling of the car, since it would tend to improve traction. However, the large unbalance in force distribution on each wheel axis also implies that most of this increased traction is directed to the rear wheels. This could in turn result in a tendency for the car to understeer with the air brake engaged. Since the crash at Le Mans 1955 occurred in a curve, such understeering could have contributed to Leveigh's inability to avoid the Austin Heley in front of him. However, the 300 SLR is known for having a large, heavy engine, meaning that a higher percentage of the total mass is located in the front of the car. This weight distribution could likely have reduced much of the effect the aerodynamic lift had on the force distribution on each axis.

### 5.4 Sources of errors

As can be seen in tables 4.1 and 4.2, the drag coefficient is significantly lower at the cases with open cooling than with closed cooling. The difference is 0.123 and 0.152 in the case with air brake down respectively up. It is expected to be lower since the air may flow through the front intake instead of stopping at the front grille. However, the difference was expected to be significantly smaller.

This unexpectedly large difference in drag coefficient could be explained by an increased flow of air through the engine compartment. It is possible that the real car

had more housings beneath the car, which means that the simplified level of detail in the engine compartment could result in misleading flow resistance. It is also possible that the inertial and viscous resistances of the radiator are set too low. This would result in too small pressure drop over the radiator, leading to a misleadingly low drag coefficient. These values are derived from earlier years bachelor thesis where they faced similar flow simulations through a radiator and could be inaccurate in this case. It would be preferable to obtain data from the manufacturer, however since this model is 60 years old the attempt to do so was unsuccessful.

During the production of the CAD-model, as described in section 3.1.2, a tool named *Multi-section surface* was used. Because of abrupt changes in the geometry the car had to be partitioned into multiple sections. One problem with this method is that an edge occur between each section. These edges or irregularities can be seen in figures 3.3 and 3.5. It is possible that some degree of flow separation is taking place at these edges. The influence of this dilemma is difficult to estimate. We expect this to increase the drag coefficient although by an insignificantly amount.

Some parts were modelled separately because the level of detail of the laser-scanned model was insufficient. The crudest simplification was made on the wheels, which were approximated as smooth with flat sides, see figure 3.5, instead of the highly detailed wheels with spokes on the real car. It is likely that the smooth wheels result in a lower drag coefficient than if the real wheels were modelled and used.

The simulations were run at 120 kph and 180 kph although the actual speed of the car at the occasion of the crash might have been up to 240 kph. This could affect the lift force on the front axis and rear axis. Increased speed is expected to result in lift force on the front and downforce on the back because of the increased moment from drag force above the wheel base. The drag coefficient however should be about the same for the different speeds.

## 5.5 Comparison with earlier works

*In order to check whether the obtained results were reasonable, they were compared to earlier works.*

The closed cooling results from the CFD simulations are recited in table 5.1 for comparison with the corresponding values presented by Gullberg and Löfdahl [1].

**Table 5.1:** Calculated values for the drag and lift coefficients and forces for the closed cooling model and corresponding results as presented by [1].

Study	Air brake	Velocity	$C_D$	$C_L$	$F_L(\text{Front})$	$F_L(\text{Rear})$
Authors'	Down	120 kph	0.273	0.257	111 N	135 N
Gullberg/Löfdahl	Down	200 kph	0.295	0.337	871 N <sup>1</sup>	347 N <sup>1</sup>
Authors'	Engaged	120 kph	0.708	-0.119	129 N	-243 N
Gullberg/Löfdahl	Engaged	200 kph	0.615	-0.013	824 N <sup>1</sup>	-871 N <sup>1</sup>

<sup>1</sup> These data are not presented explicitly in the report but can easily be calculated using given values for reference area, reference velocity and air density.

Both studies confirm the expected drag increase with the air brake engaged. Another common conclusion is the transition from positive to negative lift coefficient when raising the air brake. A negative lift coefficient indicates a downforce and, as declared by [1], explains the statements made by drivers of the SLR. The downforce generates grip and therefore the air brake must have improved the handling of the car as it was claimed by Stirling Moss, among others.

Prior to [1], the aerodynamics of the SLR were quite unknown. However, one very interesting article was published in a German motor magazine called *Motor Klassik* in 1987. Presented in this article are tests on the SLR carried out in the *Daimler-Benz* wind tunnel in Untertürkenheim in Germany. According to *Motor Klassik* a drag coefficient of 0.437 with the air brake down and 1.090 with the air brake engaged were measured in the tunnel [15]. Originally, it was planned to compare these values with the open cooling results from the CFD simulations, table 4.2, but as mentioned earlier these values are deemed to be quite unrealistic.

Comparing the closed cooling values of drag and lift coefficients, 0.237 and 0.780 respectively, measurements and simulations seem consistent. It is important to note that neither the freestream velocity nor the reference area used are presented in the *Motor Klassik* article, with means that the absolute values are not really comparable. Also, remember that in the CFD calculations rotating wheels and moving ground was simulated. This is probably not the case in the wind tunnel tests, as these were carried out in 1987.

The ratio between  $C_D$  with air brake up and  $C_D$  with air brake down for the different studies, which is independent of free stream velocity and reference area assuming that the same reference area is used with the air brake up and down. A value of 2.5 for the wind tunnel measurements and 2.6 for the CFD simulations are obtained.

Also presented in *Motor Klassik* are smoke visualisations from the wind tunnel tests, reproduced in figure 5.1. For comparison, streamlines computed in STAR CCM+ from the CFD simulations are shown in figure 5.2.

The flow pattern is fairly similar for the two different studies. Noticeable is the somewhat bigger wake in the smoke visualisations. As pointed out by [1], this can probably be explained by the slightly more angled air brake on the real car compared to the CFD-model.

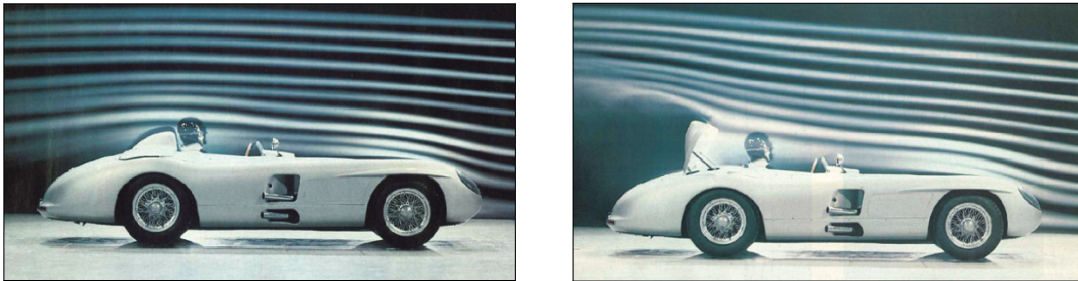


**Figure 5.1:** Smoke visualisation in the Daimler-Benz wind tunnel [15].

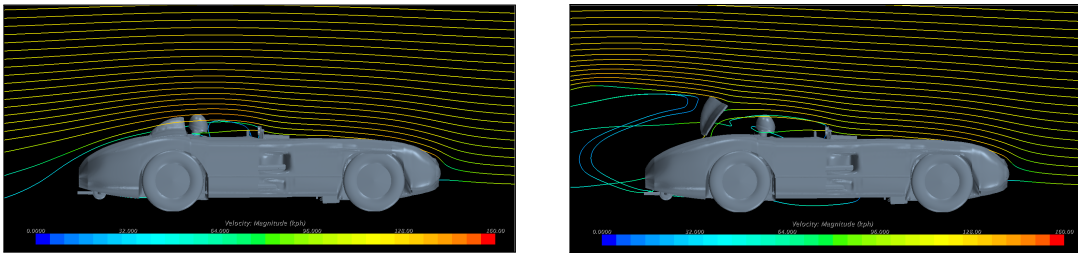


**Figure 5.2:** Computed streamlines from CFD simulations. Shown are results from the open cooling model, travelling at 120 kph. The streamlines are plotted over the cars centerline, since this seems to be the setup for the smoke visualisations.

# 6

## Conclusions

*This section summarises the project and also gives some suggestions for future works to be done on the same topic.*

### 6.1 Conclusions of this project

This thesis has focused on creating a good CAD-basis and then using CFD software to investigate the aerodynamic properties of the Mercedes-Benz 300 SLR. Due to lack of information about the undercarriage of the Mercedes, simulations were made both with a closed model and a model with open cooling.

The simulations showed a good aerodynamic performance of the Mercedes when its air brake was not in use. The simulations indicate that the air brake filled its intended purpose of improving braking. When the air brake was engaged the drag of the car was increased and a large downforce was acting on the rear wheels. This could indicate a tendency for the 300 SLR to understeer with the air brake engaged, especially at high speeds, although further analysis taking into consideration the mass distribution of the Mercedes is needed to confirm this.

The Mercedes 300 SLR seems to have had very good aerodynamic performance, and combined with its powerful engine it can be understood why it was such a superior racing machine for its time. It is a pity that the accident at Le Mans 1955 caused it to appear in such a bad manner, soiling the legacy of the 300 SLR and causing it to be remembered not for its outstanding performance but for the crash it participated in.

### 6.2 Closing remarks and future works

This project was meant to be a continuation and refinement of the work started by Löfdahl and Gullberg. Although the initial aim was to be able to investigate the aerodynamic properties of the 300 SLR not only at different velocities but also at different pitch- and yaw-angles, the limited time frame of the project did not allow this. However, a lot of time was spent on creating a good CAD-basis and meshes that will hopefully be of good use in future projects. An attempt to further improve the undercarriage is still something that could be done.

Ideas for further projects on the 300 SLR could be to make the simulations of different pitch, yaw and velocities that could not be done this year, in order to further analyse the air brake's effect on breaking and cornering performance. Especially studies of higher speeds could be of interest, as when the 1955 Le Mans crash took place the car's speed was around 240 kph. As mentioned above it could also be of interest to take the mass distribution of the Mercedes in consideration during simulations to gain better insight in how this affected the handling of the car. Another possible project could be to focus more on the Le Mans crash and attempt to create an improved model of the flight of the 300 SLR after the impact, taking into account the aerodynamic properties of the car, which in turn would be a continuation of another work by Löfdahl and Gullberg [16].

# Bibliography

- [1] P. Gullberg and L. Löfdahl. The Role of Aerodynamics in the 1955 Le Mans Crash. Technical Report 2008-01-2996, SAE Technical Paper Series, 2008.
- [2] C. Hilton. *Le Mans '55: The crash that changed the face of motor racing*. Breedon Books Publishing, 2004. ISBN 1 85983 441 8.
- [3] Deadliest Crash: the Le Mans 1955 Disaster, BBC Four documentary, broadcast 16 May 2010, <https://www.youtube.com/watch?v=j0RfHIjgr0c>.
- [4] Automobile catalog. Specifications 1955 Mercedes-Benz 300 SLR. <http://www.automobile-catalog.com>. [Accessed 2015-04-27].
- [5] M. White. *Fluid Mechanics*. McGraw Hill Higher Education, New York, 7th edition, 2011.
- [6] J. Katz. *Race Car Aerodynamics: Designing for Speed*. Bentley Publishers, Cambridge, MA, 1995.
- [7] A. J. Smits et al. Drag of Blunt and Streamlined bodies. [http://www.princeton.edu/~asmits/Bicycle\\_web/blunt.html](http://www.princeton.edu/~asmits/Bicycle_web/blunt.html). [Accessed 07 april 2015].
- [8] T.-H. Sikh et al. A New  $k$ - $\epsilon$  Eddy Viscosity Model for High Reynolds Number Turbulent Flows - Model Development and Validation. Technical Report NASA-TM-106721, Institute for Computational Mechanics in Propulsion and Center for Modeling of Turbulence and Transition, Lewis Research Center, Cleveland, Ohio, August 1994. <http://ntrs.nasa.gov/archive/nasa/casi.ntrs.nasa.gov/19950005029.pdf>.
- [9] M. Subhendu and W. Hari. Reynolds Stress Anisotropy Based Turbulent Eddy Viscosity Model Applied to Numerical Ocean Models. *J. Fluids Eng.* 133(6), 064501 (2011) (3 pages); doi:10.1115/1.4004216.
- [10] J. Geertsma. Estimating the Coefficient of Inertial Resistance in Fluid Flow Through Porous Media. Technical report, KONINKLIJKE/SHELL EXPLORATIE EN PRODUCTIE LABORATORIUM, RIJSWIJK, THE NETHERLANDS, 1979. [Accessed 2014-04-28].
- [11] H. Ström. Boundary layer theory. Lecture notes, Chalmers University of Technology, 2014.

- [12] Carfolio.com, <http://www.carfolio.com/specifications/models/car/?car=61941>, [Accessed 2015-05-14].
- [13] BETA CAE Systems S.A, Thessaloniki, Greece. *ANSA v.14.x Tutorials, External Aerodynamics*. [Accessed 2015-04-28].
- [14] J. Bondesson et al. Comparisons of the Aerodynamic Performance of two Silver Arrows from the Thirties. Bachelor Thesis in Applied Mechanics, Chalmers University of Technology, 2014.
- [15] *Motor Klassik*, (3):10–11, 1987.
- [16] L. Löfdahl, P. Gullberg, and Z. Qiu. Influence of Aerodynamics on the Fatal Crash in Le Mans 1955. Technical report, European Automotive Simulation Conference, 2009.

# A

## CAD models

*This appendix contains images of the CAD-models which were used in the simulations.*

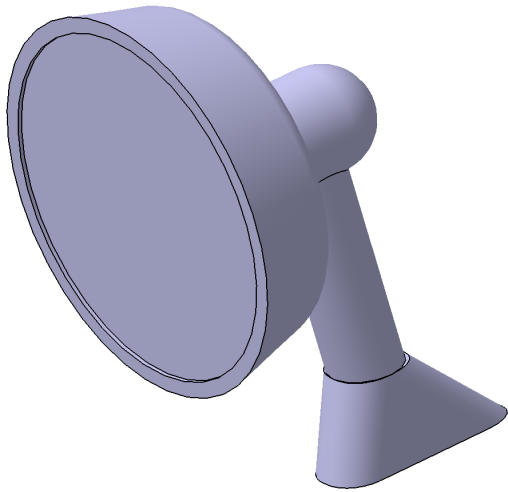


**Figure A.1:** Rear-view mirror.

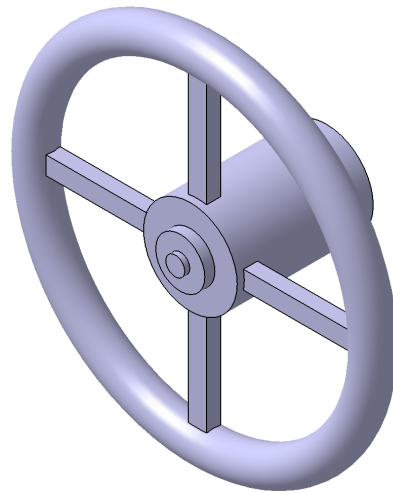


**Figure A.2:** Steering wheel.

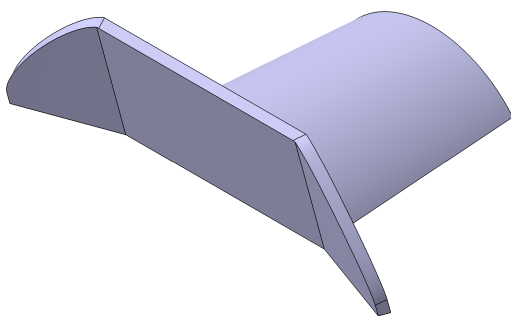


**Figure A.3:** Windshield.

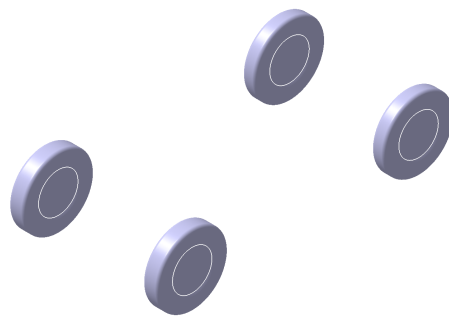


**Figure A.4:** Wheels.

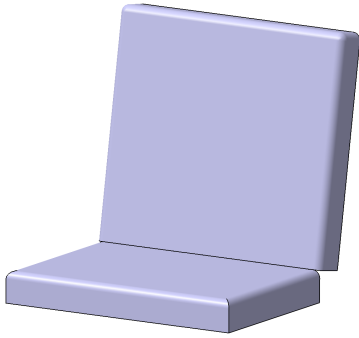


**Figure A.5:** Seat.



**Figure A.6:** Headlights.



**Figure A.7:** Driver.

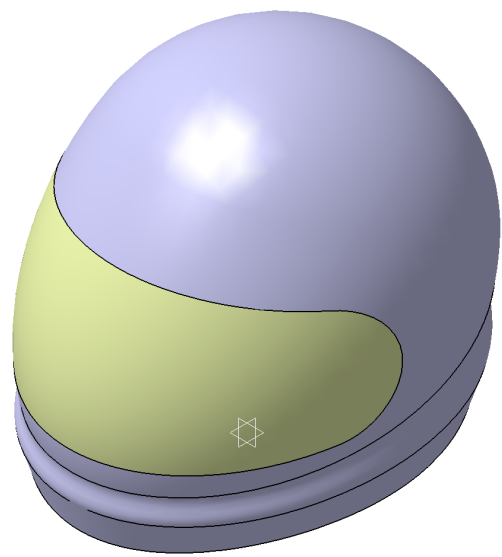


**Figure A.8:** Helmet.

# B

## PID's

*This appendix lists all the PID's (Property ID's) included in the final model of the Mercedes-Benz 300 SLR.*

Id	Name
25	Air-brake_edge
8	Air-brake_high
21	Air-brake_low
27	Body
7	Chassis
10	Cockpit
18	Driver
4	Engine_and_fuel
15	Exhaust_pipes
17	Front_grille
3	Front_suspension
20	Front_wheels
16	Headlights
13	Helmet
24	Radiator
26	Radiator_plane
12	Rearview_mirror
6	Rear_suspension
19	Rear_wheels
11	Seat
9	Steering_wheel
23	Stripes
5	Transmission
22	Underbody
14	Visor
2	Windshield
1	Windshield_cap

PROPERTY total 27 selected 0

